High-Pressure Phase Transitions of Morphologically Distinct Zn₂SnO₄ Nanostructures

Partha Pratim Das,[†][iD] P. Sujatha Devi,[‡][iD] Douglas A. Blom,[§] Thomas Vogt,[∥] and Yongjae Lee[*,†,⊥][iD]

[†]Department of Earth System Sciences, Yonsei University, Seoul 120749, Korea

[‡]Sensor and Actuator Division, CSIR-Central Glass and Ceramic Research Institute, Kolkata 700032, India

[§]NanoCenter & Department of Chemical Engineering, and [∥]NanoCenter & Department of Chemistry & Biochemistry, University of South Carolina, Columbia, South Carolina 29208, United States

[⊥]Center for High Pressure Science and Technology Advanced Research, Shanghai 201203, China

ⓢ *Supporting Information*

ABSTRACT: Many aspects of nanostructured materials at high pressures are still unexplored. We present here, high-pressure structural behavior of two Zn₂SnO₄ nanomaterials with inverse spinel type, one a particle with size of ∼7 nm [zero dimensional (0-D)] and the other with a chain-like [one dimensional (1-D)] morphology. We performed in situ micro-Raman and synchrotron X-ray diffraction measurements and observed that the cation disordering of the 0-D nanoparticle is preserved up to ∼40 GPa, suppressing the reported martensitic phase transformation. On the other hand, an irreversible phase transition is observed from the 1-D nanomaterial into a new and dense high-pressure orthorhombic CaFe₂O₄-type structure at ∼40 GPa. The pressure-treated 0-D and 1-D nanomaterials have distinct diffuse reflectance and emission properties. In particular, a heterojunction between the inverse spinel and quenchable orthorhombic phases allows the use of 1-D Zn₂SnO₄ nanomaterials as efficient photocatalysts as shown by the degradation of the textile pollutant methylene blue.
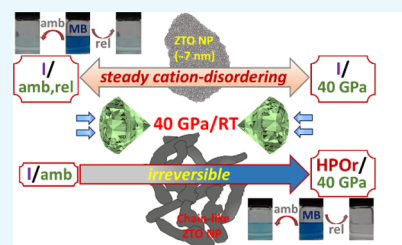
■ INTRODUCTION

The distinct behaviors of nanostructured materials from those of their bulk counterparts are the prime motivation behind research on nanomaterials in various fields.[1−5] The interplay among particle sizes of the building blocks in the nanoregime, the different atomic structures, and the surface and interfacial properties of the grains are the deciding factors in the distinctive functional behavior of nanomaterials.[6−8] In the pursuit of new phenomena in nanomaterials, high pressure has been employed recently to modify the atomic arrangements and interactions of materials.[9−14] Understanding the pressure-induced structural stability of various types of nanomaterials and the concomitant tuning of their physicochemical properties is important from both a fundamental and application point of view.

Over the past few decades, semiconducting nanomaterials of different types and structures have greatly contributed to significant progress in nanoscience and technology due to their salient and flexible opto-electronic, photonic, magnetic, and mechanical features.[15−19] As far as the exploration of semiconducting nanomaterials under high pressure is concerned, studies on a variety of materials, namely, the group (IV) elements C, Si, and their compound SiC; group (II−VI) compounds such as ZnS, ZnSe, CdS, CdSe, and CdTe; group (IV−VI) PbS; group (III−V) GaN and AlN; the superhard material, BC₂N; binary oxides such as TiO₂, ZnO, SnO₂, Fe₂O₃, and CeO₂; the rare-earth oxide, Ho₂O₃; wide band-gap oxides such as β-Ga₂O₃ and Y₂O₃; p-type compounds

including CuO, CoO, and MnS; n-type BaTiO₃; and narrow band-gap layered group (V−VI) semiconductors such as Bi₂Te₃, have been performed.[9,10,12,14,20−38] Most of these studies have shed light on the interesting kinetics of pressure-induced first-order, solid−solid structural transformations, compressibilities, bulk moduli, and stiffness or hardness of the materials.[23−31] The thermodynamics of phase transformations and relative stabilities of the phases have also been noted in several studies.[24−26,30−33] Although there are conflicting trends in the reported transition pressures relating to the Hall−Petch effect that is found as bulk materials are reduced to smaller crystallites, a significant influence from nanosized particles or grains has been commonly suggested as the cause for the dissimilar types of nucleation, growth dynamics, phase transition pathways, and even sequences of the phase transitions or amorphizations of semiconducting materials under high pressure.[31,32,34,35] A specific size, at which the typical nanoscale effects start to occur in materials, has also been defined as their respective "critical size" in several cases.[27,32,34] The contributions of the nanoscale-induced differences in the surface energies of the relevant phases mainly account for the stabilities of the corresponding structures.[24,33] In this context, the impacts of various microstructural features, for instance, the distinct shape or
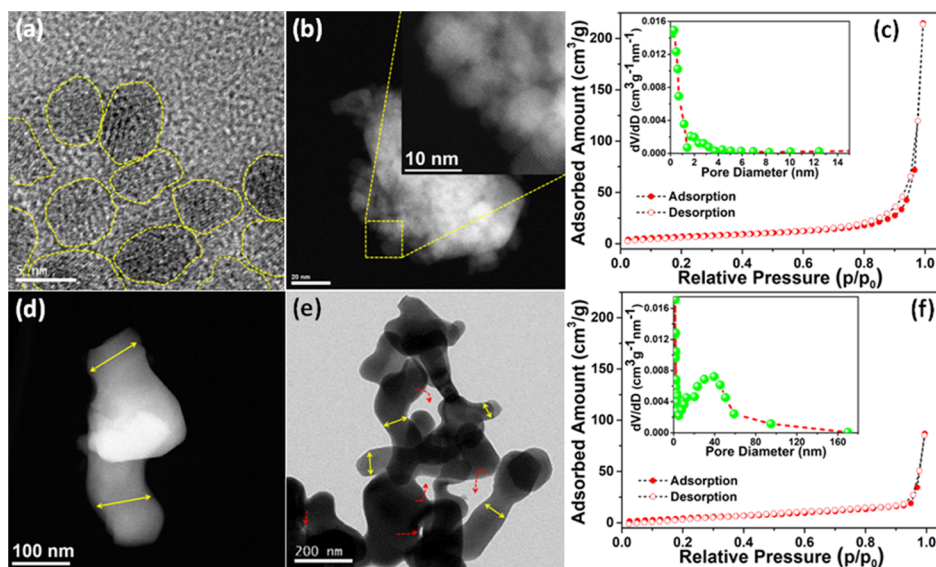
Figure 1. (a) TEM and (b) STEM image of the 0-D Zn_2SnO_4 nanoparticles, (d) STEM and (e) TEM image of the 1-D Zn_2SnO_4 nanostructures, and (c,f) N_2 adsorption−desorption isotherms of the 0-D Zn_2SnO_4 nanoparticles and 1-D Zn_2SnO_4 nanostructures, respectively. The insets exhibit their PSDs.

morphology, dimension, and homogeneity, of the materials are often found to coincide with the size effects of the nanocrystals in many studies.[9,14,33,36−39] The microstructure-induced strains appearing at the contact points of the grains of the materials may cause significant structural distortions, which also contribute to the transition pressure and phase stability.[8,14]

In the present study, the simultaneous effects of the size and microstructure have been investigated on the high-pressure phase transition of a specially designed ZnO−SnO₂-based multi-cation oxide, Zn_2SnO_4. The wide band gap, n-type semiconducting Zn_2SnO_4 is highly acclaimed as a potential candidate for various applications, such as dye-sensitized solar cells, transparent conducting oxides, photocatalytic degradation, humidity and combustible gas sensing, and Li-ion batteries.[40−43] However, the high-pressure behavior of this important material has hardly been explored. A single theoretical study by Gracia et al. highlighted the structural, electronic, and optical properties of bulk Zn_2SnO_4.[44] Based on their work, the pressure-induced phase transition of spinel Zn_2SnO_4 to orthorhombic phases was identified to be of the $CaTi_2O_4$ (titanite-type) and $CaFe_2O_4$ (ferrite-type) structures at 39 and 54 GPa, respectively, and then the Sr_2PbO_4 structure at higher pressure. Shen et al., first experimentally detected the formation of an orthorhombic, ambient pressure $CaFe_2O_4$-like structure at ∼32 GPa through an intermediate orthorhombic phase at ∼13 GPa in Zn_2SnO_4 nanowires with a diameter of approximately 150 nm.[45] In a separate study, an entirely different phase transition from the cubic to hexagonal phase at ∼30 GPa for single-crystal Zn_2SnO_4 having a tetrakaidecahedral morphology and an average particle size of 800 nm was reported by Zhang et al.[11] They also mentioned a variation in the electrical resistance due to a reduction of the Zn_2SnO_4 micrograins to nanocrystals of approximately 5 nm at ∼13 GPa, where remarkably, no structural transition was observed. Therefore, the variety of the observed properties, even in these very limited number of studies, unequivocally motivated us to further study the high-pressure behavior of this semiconducting oxide with distinct sizes and microstructures. "Zero" dimensional (0-D) nanoparticles, with a size of ∼7 nm, as well

as unique "one" dimensional (1-D), dense, and elongated Zn_2SnO_4 nanostructures, with an average grain width of ∼100 nm, have been used in this study. Both samples were characterized before and after the pressure treatments based on their optical properties and efficiencies for photocatalytic degradation of the well-known textile dye methylene blue (MB).

The ternary oxide, Zn_2SnO_4, which has cubic ($Fd3m$) symmetry, belongs to the $(A^{2+})[B^{4+}A^{2+}]O_4$-type inverse spinel oxides in the bulk state, where half of the A cations populate the tetrahedral sites and the other half occupy the octahedral sites along with all of the B cations.[46] Several spinel oxides possess complicated disordering phenomena involving the redistribution of cations A and B over the tetrahedrally and octahedrally coordinated sites. There have been reports claiming a significant role of this cation reordering in spinel oxides with regard to the structural stability and diffusional or diffusionless phase transformations at high temperatures.[47−49] Few studies have highlighted a similar phenomenon for several bulk spinel oxides at high pressure.[47−49] The Zn_2SnO_4 nanoparticles with grain sizes of ∼7 nm used in this present study reveal cation disorder. Therefore, this represents a unique occasion to characterize the phase transformations associated with cation reordering of a nanosized inverse spinel oxide, which is another important aspect of the present study.

RESULTS AND DISCUSSION

Microstructural and Optical Characterizations of the Samples under Ambient Conditions. A bright field transmission electron microscopy (TEM) image of the hydrothermally synthesized Zn_2SnO_4 sample dispersed in ethanol is presented in Figure 1a. The high-resolution image shows the monodispersed spherical particles with sizes of less than 10 nm in all dimensions. The particles are marked with yellow dotted lines for a clear demarcation. At the same time, the 0-D nanoparticles are found to be aggregated in the final Zn_2SnO_4 sample studied here as revealed by the high-angle annular dark-field-scanning TEM (HAADF-STEM) images in Figure 1b. As a consequence, a moderate surface area of
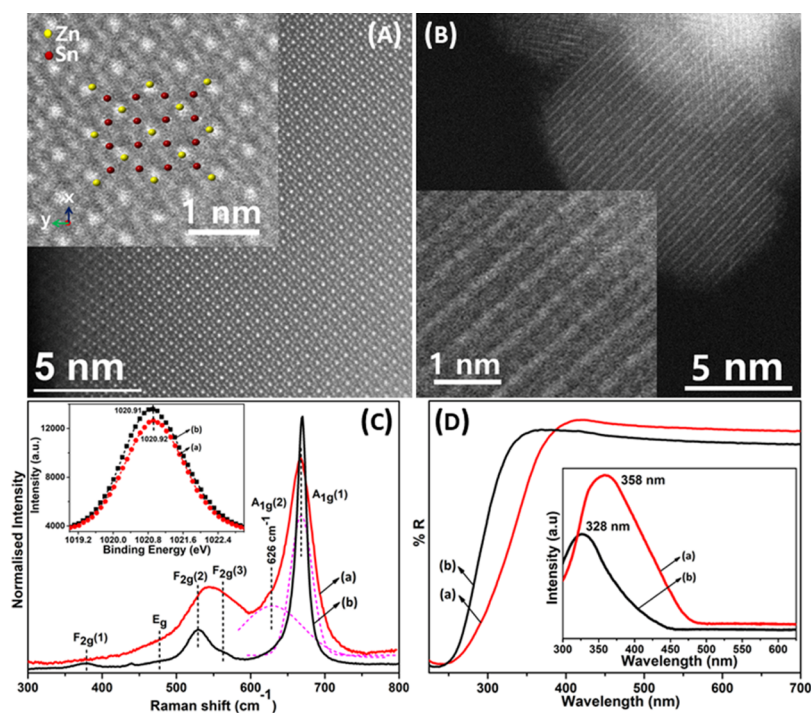
Figure 2. (A) HAADF-STEM image of the 1-D Zn_2SnO_4 nanostructures, inset shows the superimposed inverse spinel crystal structure, (B) HAADF-STEM image of the 0-D Zn_2SnO_4 nanoparticles with an inset showing higher resolution image of disordered Zn and Sn sites, (C,D) Raman spectrum and DR spectrum of (a) 0-D Zn_2SnO_4 nanoparticles and (b) 1-D Zn_2SnO_4 nanostructures, respectively. Inset of (C,D) represents the XPS and emission spectra of each, respectively.

~36.71 m^2/g was obtained for the Zn_2SnO_4 nanoparticles prepared by the hydrothermal method from the Brunauer–Emmett–Teller (BET) analysis. In addition, the characteristic type-III isotherm that is observed in the N_2 adsorption–desorption studies (Figure 1c) along with an insignificant pore size distribution (PSD) as calculated by the Barrett–Joyner–Halenda (BJH) method (Figure 1c, inset) further support the nonporous nature and compactness of the nanoparticles of the Zn_2SnO_4 sample.

The Zn_2SnO_4 sample prepared from the temperature-assisted solid-state reaction between ZnO and SnO_2 appears to have a self-assembled elongated chain-like unique morphology. The STEM image of a small unit of the typical chain-like particles of Zn_2SnO_4 and the TEM image that includes several similar particles assembled together are displayed in Figure 1d,e, respectively. The actual width of the individual chain-like particles measured considering only their nonoverlapping sections varies over the range of 50−100 nm (marked with yellow double arrows). The dark contrast in both the STEM and TEM images of the 1-D particles indicates that the Zn_2SnO_4 nanostructures formed by the solid-state method are highly dense in nature and have no Kirkendall pores.[41] This, again, is supported by the type-III N_2 adsorption−desorption isotherm exhibited by the dense Zn_2SnO_4 nanostructures (Figure 1f). The BET surface area obtained from the sample was found to be very low at ~4.23 m^2/g. However, the BJH PSD, shown in the inset of Figure 1f, contrarily reveals the presence of pores with a wide distribution of sizes varying from ~5 to ~60 nm even in these dense Zn_2SnO_4 nanostructures. The intergrain voids (marked with red arrows) among the chain-like particles assembled with each other, and that assembly should be the only source of introducing meso- to microporosity in the sample (Figure 1e),

which makes this particular morphology more exceptional for studying at high pressure.[41,43]

The order−disorder phenomena in the local structures of the samples were verified using HAADF-STEM real-space imaging. A high-resolution HAADF-STEM image from the 1-D Zn_2SnO_4 nanostructures viewed along the (100) direction is displayed in Figure 2a. The inverse-spinel crystal structure of Zn_2SnO_4 (x, y, z = 1 unit) that is superimposed on the experimental HAADF-STEM image matches with the Z-sensitive contrast of the Zn and Sn columns that define the ordered distribution of Zn^{2+} and Sn^{4+} over the lattice sites (Figure 2a, inset). The sites with brighter contrast in the image, marked with yellow balls, correspond to the Sn atoms, which have a higher atomic number (Z) compared to Zn, and the sites of the Zn atoms are marked with red balls. In contrast, the HAADF-STEM image of the 0-D nanoparticles showed significantly lower contrast. This interesting phenomenon suggests a lack of ordering between the Zn and Sn sites in the hydrothermally synthesized Zn_2SnO_4 nanoparticles. The possibility of a redistribution of Zn^{2+} and Sn^{4+} in the octahedral and tetrahedral crystal sites of the inverse spinel Zn_2SnO_4 is considered, in this regard, as an effect of the reduction of particle size because we have <10 nm particle sizes.[46] The imperfect alignment of the Zn and Sn columns as related to the aforementioned disorder may lead to the low contrast observed in the HAADF image.[46,51,52] The distorted local structure of this particular 0-D nanosized Zn_2SnO_4 was further confirmed from its unusual Raman phonon $A_{1g}(2)$ mode at ~626 cm^{-1}, which is the characteristic vibrational mode for a nonequilibrium cation distribution in the inverse spinel structure (Figure 2c).[46,50] The other Raman active bands seen in Figure 2c can be attributed to the $A_{1g}(1)$, $F_{2g}(3)$, $F_{2g}(2)$, E_g, and $F_{2g}(1)$ symmetries of the typical inverse spinel
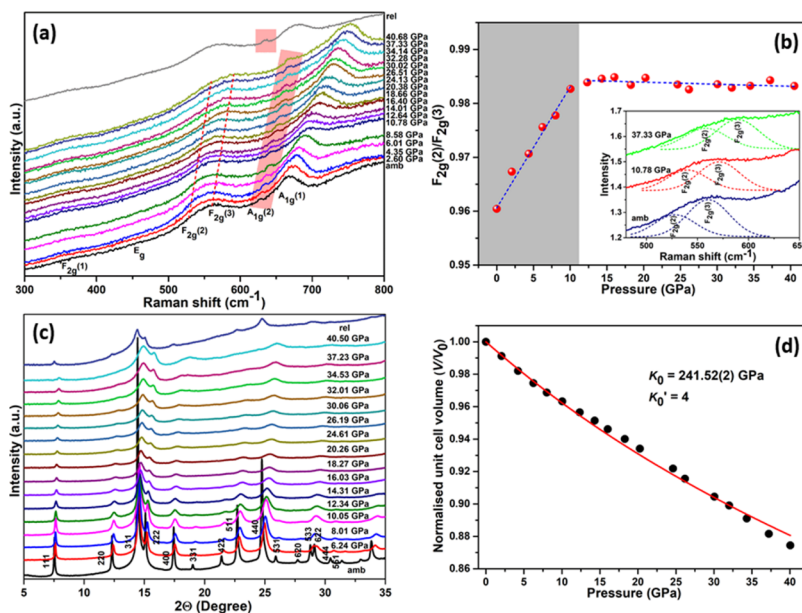
Figure 3. (a,c) Pressure-dependent Raman spectra and XRD of the 0-D Zn_2SnO_4 nanoparticles, (b) variation in the ratio of the $F_{2g}(2)$ and $F_{2g}(3)$ peaks as a function of pressure, inset shows the deconvoluted $F_{2g}(2)$ and $F_{2g}(3)$ peaks of the Raman spectra at selective pressure conditions, and (d) fitting of V/V_0 using the Birch–Murnaghan equation of state.

structure of Zn_2SnO_4 and appeared at similar positions for both samples.[41,46] The measured ratio of the intensity of the $F_{2g}(2)$ and $F_{2g}(3)$ bands of the 1-D nanoparticles with peaks at ~529 and 559 cm^{-1} is 1.3:1. However, the same with an inverse intensity order ($F_{2g}(2)/F_{2g}(3)$ = 1:1.042) indicates the possibility of higher [B] site populations of Zn^{2+} instead of Sn^{4+} in the 0-D Zn_2SnO_4 nanoparticles.[46] Moreover, the exceptionally broad Raman spectral lines further suggest that the 0-D Zn_2SnO_4 nanospinel has a deformed MeO_6 octahedra as well as MeO_4 tetrahedra (Me = Zn or Sn).[46] To eliminate the likelihood of any chemical disorder in this case, the chemical compositions of the samples were compared with a reported mixture of ZnO and SnO_2 at a ratio of 2:1, based on the X-ray photoelectron spectroscopy (XPS) analysis. It is worth mentioning that the Zn $2p_{3/2}$ spectra of both Zn_2SnO_4 samples studied here are found to be nearly identical to that of the standard mixture with respect to the positions of their binding energies (~1020.92, ~1020.91, and ~1021.4 eV for the 0-D nanoparticles, 1-D nanostructures and the standard mixture, respectively) and symmetric spectral shapes, as represented in the inset of Figure 2c.[46] This elucidates that the samples, even though synthesized by different methods, are chemically homogeneous with an atomic ratio of 2 for Zn to Sn. The XPS investigation also confirms the influence of no chemical disorder on the nonuniform structure of the 0-D Zn_2SnO_4 nanoparticles.

Therefore, based on the HAADF, Raman, and XPS analyses, it can be stated that, while the 1-D Zn_2SnO_4 nanostructures have the inverse spinel structure, the cation distribution in the 0-D nanoparticles have a partially inverse spinel structure with the chemical formula $(Zn_\delta Sn_{1-\delta})^{tet}[Sn_\delta Zn_{2-\delta}]^{oct}O_4$, where the value of the inversion parameter, "δ" is between 0 and 1.[46] A decrease in the optical band gap from ~3.85 to ~3.51 eV was estimated from the redshifted absorption edge in the diffuse reflectance (DR) of the 0-D nanoparticles compared to that of the 1-D nanostructures yet having the larger particle sizes, as exhibited in the inset of Figure 2d. This observation corroborates the first principles study performed by Wei et

al. on the anomalous band gap reduction as a function of the cation inversion for $SnB^{II}_2O_4$-type spinel oxides, such as Zn_2SnO_4.[53] The emission properties of the as-prepared samples were measured thereafter (Figure 2d, inset). The emission maxima appeared at ~328 nm for the 1-D nanostructures, whereas that for the 0-D nanoparticles shifted to the mid-UVA region at ~358 nm. The observed emissions of both Zn_2SnO_4 samples refer to their intraband electron transitions only.

0-D Zn_2SnO_4 Nanoparticles under High Pressure: Effects of Size. The pressure-induced structural behavior of the 0-D nanosized Zn_2SnO_4 accompanying the nonequilibrium structure was investigated by in situ Raman and X-ray diffraction (XRD) studies. Based on earlier reports, we anticipated an order–disorder-mediated structural transformation in these studies. Therefore, the variation in the relative intensities of the $A_{1g}(2)$ (red shaded area, Figure 3a) and $F_{2g}(2)$ modes versus that of the $F_{2g}(3)$ mode was monitored at elevated pressures as shown in Figure 3b. The impact of high pressure on cation reordering was negligible because there is no significant pressure-dependent change in the intensity of the $A_{1g}(2)$ peak. The $F_{2g}(2)/F_{2g}(3)$ ratio remained almost constant as well, up to ~40 GPa, after a minute initial enhancement at ~8−10 GPa. The $F_{2g}(2)$ and $F_{2g}(3)$ peaks obtained by multipeak fitting of the Raman spectrum at ambient, ~10 and ~37 GPa are displayed in the inset of Figure 3b. An indisputable stress arises to make more compact contact between the spherical nanograins and may have induced some disorder at lower pressure (also discussed later). However, unperturbed structural disorder under high pressure usually leads to a martensitic phase transformation through a diffusionless mechanism, which should promote the possibility of a faster phase transition in spinel structures, such as Zn_2SnO_4.[47−49] In contrast, no salient modification in the Raman modes indicating a new phase are observed for the sample up to ~40 GPa, except for a regular shift of the bands toward higher frequencies (Figure 3a). This exceptional behavior of the 0-D Zn_2SnO_4 nanoparticles is further
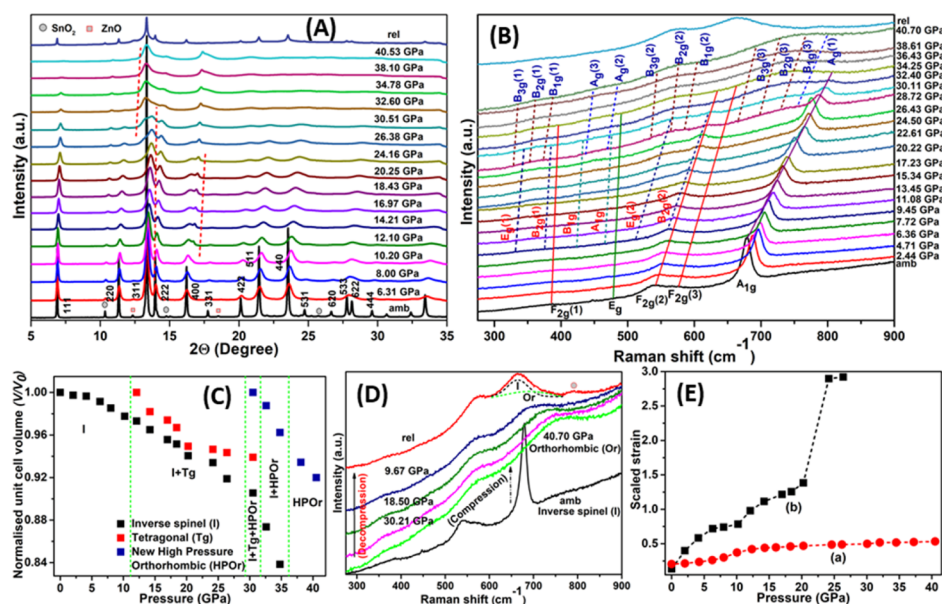
Figure 4. (A,B) Pressure-dependent XRD and Raman spectra of the 1-D Zn_2SnO_4 nanostructures, (C) variations in V/V_0 of the evolved phases with pressure, (D) Raman spectra of the 1-D Zn_2SnO_4 nanostructures during decompression and (E) comparison of the calculated strains for (a) 0-D Zn_2SnO_4 nanoparticles and (b) 1-D Zn_2SnO_4 nanostructures.

confirmed by the XRD patterns shown in Figure 3c, which exhibit only a systematic pressure-induced shift in the 2θ values toward higher angles along with certain peak broadening. A significantly high bulk modulus (B_0) of ~241.52(2) GPa can be determined, thereafter, using the second-order Birch–Murnaghan equation of state, where K_0' is fixed at 4 (Figure 3d).[12] Therefore, the 0-D small ~7 nm particles are stable and do not undergo a martensitic transformation. This study introduces diffusionless cation reordering as an important size effect during the pressure-induced phase transformation of this spinel oxide. Further studies are underway to determine whether there is any "critical size" for the Zn_2SnO_4 nanoparticles, where the cation disorder in the structure persists, while at the same time influencing either the diffusional or diffusionless phase transformation at higher pressures.

1-D Zn_2SnO_4 Nanostructures under High Pressure: Effects of Morphology. The pressure-dependent structural transformation of the 1-D Zn_2SnO_4 nanostructures with an elongated chain-like morphology was explored using the same pressure range of up to ~40 GPa. Interestingly, two successive modifications of the inverse spinel structure of the sample at ambient conditions (space group: $Fd3m$; calculated lattice parameter: $a = 8.66(1)$ Å) can be seen in the XRD patterns as a function of pressure, shown in Figure 4A. (The small impurities of ZnO (square shaped mark) and SnO_2 (round shaped mark) are not considered in the analysis). First, a splitting of the diffraction peak corresponding to the (400) plane into two peaks was found to begin at ~10 GPa, which can be attributed to a tetragonal distortion of the cubic inverse spinel structure. The lattice parameters calculated by whole-profile fitting of the corresponding XRD pattern are $a = 8.58(3)$ Å and $a = b = 6.09(1)$ Å, $c = 8.50(1)$ Å for the inverse spinel and tetragonal structures, respectively. The distortion became stronger with increasing pressure up to ~26 GPa. The analogous distortion, albeit ambiguously characterized as an intermediate phase by Shen et al., was followed by a further phase transition to the ambient-pressure structure of

orthorhombic $CaFe_2O_4$ at ~32 GPa for the Zn_2SnO_4 nanowires with an average diameter of ~150 nm.[45] Similarly, the onset of a second phase transition can also be observed at ~30 GPa for the chain-like Zn_2SnO_4 with an average width of ~100 nm, indicating a comparable surface area-to-volume ratio to that of the Zn_2SnO_4 nanowires studied by Shen et al.[39,45] However, it is worth noting that a new denser high-pressure orthorhombic $CaFe_2O_4$ structure appeared, which is equivalent to the $CaFe_2O_4$ structure that occurred at ~63 GPa, as reported by Yamanaka et al.[54] The analysis by Yamanaka et al. provides the same $Pnma$ space group symmetry but with a three-fold larger c-axis dimension ($c = 8.353(1)$ Å) for this new phase compared to that of the orthorhombic $CaFe_2O_4$ structures that appear at lower pressures. For instance, the calculated values for "c" are 2.889(3) and 3.019(2) Å at ~42 and 0.0001 GPa, respectively. An identical "c", 8.448(6) Å corresponding to the new phase, was obtained in our case for the chain-like Zn_2SnO_4 nanostructures by whole-profile fitting analysis of the XRD pattern at ~30 GPa. The complete transformation into the new phase ($c = 8.347(2)$) is found to take place at ~38 GPa through the gradual disappearance of the tetragonal structure at ~32 GPa followed by the inverse spinel structure at ~34 GPa. The high pressure phase of the orthorhombic $CaFe_2O_4$-type structure is quenchable and exhibits an irreversible phase transition even after releasing the pressure. The normalized unit cell volumes of the consecutive phases are shown in Figure 4C. The whole-profile fitting of the selective XRD patterns mentioned above are represented in Figure S1a−d. To the extent of our knowledge, this is the first observation of the transformation of the inverse spinel structure of Zn_2SnO_4 into a much denser high-pressure $CaFe_2O_4$-type structure.

The pressure-induced phase transformations observed from the XRD analysis of the elongated chain-like Zn_2SnO_4 nanostructures were further verified by in situ Raman spectroscopic study (Figure 4B). Primarily, a substantial shift can be observed for the five first-order Raman active modes, $A_{1g}(1)$, $F_{2g}(3)$, $F_{2g}(2)$, E_g, and $F_{2g}(1)$, representing the cubic
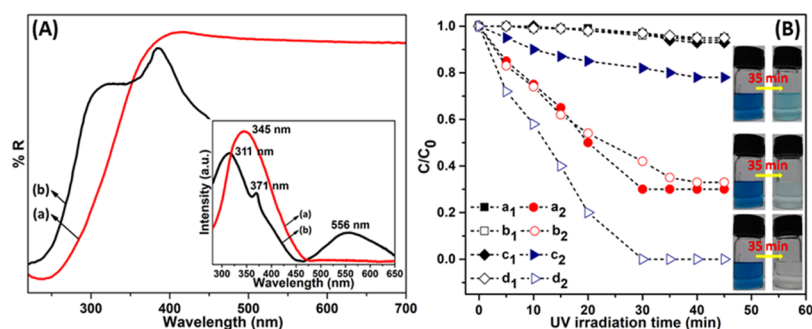
Figure 5. (A) DR spectra of the 0-D Zn_2SnO_4 nanoparticles and (b) 1-D Zn_2SnO_4 nanostructures after the pressure is released. Inset represents their corresponding emission spectra. (B) Comparative photodegradation profiles of MB in the presence of (a_2) as-prepared and (b_2) recovered 0-D Zn_2SnO_4 nanoparticles, (c_2) as-prepared and (d_2) recovered 1-D Zn_2SnO_4 under UV irradiation. (a_1–d_1) indicate the same in the absence of the samples.

inverse spinel structure of Zn_2SnO_4 in the $Fd3m$ space group to higher frequencies as the pressure was increased to ∼9 GPa. A distinctive broadening of all three F_{2g} and E_g modes is observed at ∼11 GPa. This evidence supports a breaking of the degeneracy by the transformation of F_{2g} into (B_{2g} + E_g) and E_g into (A_{1g} + B_{1g}) modes, the characteristic Raman modes of the lower-symmetry tetragonal structure of the $I4_1/amd$ space group.[45,55] Similar to the XRD results, the bands corresponding to the tetragonal phase became more intense up to ∼26 GPa. The appearance of a broad band with maxima at ∼725 cm^{-1} along with the broadening of the other bands, mainly the E_g (tetragonal) band, confirm a further lowering of the symmetry and the onset of the orthorhombic $CaFe_2O_4$-type structure of the $Pnma$ space group at ∼28 GPa, whereas complete conversion into the purely orthorhombic phase occurred at ∼36 GPa.[45,55] The Raman study comprehensively confirms the XRD analysis, whereas the recovered sample also exhibits the residual modes of the orthorhombic $CaFe_2O_4$-type structure (Figure 4D). However, it has not escaped our notice that an unusual mode at ∼790 cm^{-1}, marked with round shape, can be observed in the recovered sample, which might be a result of the partial disorder in the sample (Figure 4D).[48]

First, formation of the high-pressure orthorhombic $CaFe_2O_4$-type structure, yet having a comparable cohesive energy to that in the previous study, followed by disordering in the structure highlights the involvement of a high amount of strain during the pressure-induced phase transformation of the 1-D Zn_2SnO_4 nanostructures. The typical chain-like grains, which have several uneven inter grain voids (as depicted from the TEM image and BET study in Figure 1e,f), may induce extreme stress at the contact points among the grains.[8,14] The inhomogeneous distribution of the stress with increasing pressure and the consequent microstrain developed at the grain boundaries are considered to play a crucial role in the phase transformation pathway of the Zn_2SnO_4 nanostructures.[8] In this regard, the pressure-induced evolution of the microscopic strain based on the major (311) diffraction peak of the inverse spinel phase is also determined for the 1-D Zn_2SnO_4 nanostructures using the Stokes–Wilson equation[12] and is compared with that of the 0-D nanoparticles having a nonporous and compact distribution of spherical particles mentioned earlier (Figure 4E). After an initial densification, the strain remained almost homogeneous for the 0-D Zn_2SnO_4 nanoparticles. In contrast, a much higher strain, which constantly increased with pressure and reached a maximum value at the onset pressure of the orthorhombic $CaFe_2O_4$

phase at ∼28 GPa, can be seen for the Zn_2SnO_4 sample having a chain-like morphology. A similar trend in the microstrain was also observed based on the (111), (220), (511), and (440) diffraction planes, as represented in Figure S2. The notable jump in the microstrain at ∼10 GPa (Figures 4E and S2) may be attributed to grain refinement of the chain-like Zn_2SnO_4 nanostructures, similar to that reported by Zhang et al.[11]

Optical Characteristics of the Recovered Samples: Comparison of Their Photocatalytic Activities. The pressure-dependent modifications of the Zn_2SnO_4 samples were further isolated by successive verification of their band gaps and emission properties after the pressure was released. Only a small blueshift of ∼10 nm was found in the absorption edge of the DR spectrum and, accordingly, in the emission maxima of the recovered 0-D Zn_2SnO_4 nanoparticles (Figure 5A) compared to those of the ambient sample. This result suggests an extensive effect of the pressure-induced increase in the direct band gap of the spinel Zn_2SnO_4 structures, as reported by Gracia et al.[44] However, an additional absorption edge of ∼368 nm with a much lower band gap of ∼3.37 eV was observed for the recovered 1-D Zn_2SnO_4 nanostructures along with the inverse spinel phase, which results in a higher band gap of ∼4.19 eV compared to the as-prepared sample (∼3.85 eV). The low energy absorption in this case can be unequivocally considered to originate from the orthorhombic phase. Interestingly, the broad emission from the UV to visible region corresponding to this particular sample exhibits three maxima. An intense peak at ∼311 nm followed by a broad peak at ∼371 nm can be assigned to the respective band edge emissions of the inverse spinel and orthorhombic phases. Moreover, a broad visible band centered at ∼556 nm may originate from the strain-induced disorder in the chain-like Zn_2SnO_4 nanostructures, as observed in the Raman spectrum. The as-prepared Zn_2SnO_4 samples were compared with their respective recovered counterparts in regard to their efficiencies as photocatalysts toward the degradation of a model organic pollutant, MB, under UV illumination (365 nm, 8 W). The comparative degradation profiles of the characteristic absorption at 665 nm of MB over time are shown in Figure 5B, where C_0 and C indicate the concentrations of MB before and after UV exposure, respectively. The rate of photodegradation efficiency is significantly altered after 35 min of UV irradiation in the order 1-D Zn_2SnO_4 nanostructures$_{as\ prepared}$ (E_g: ∼3.85 eV) < 0-D Zn_2SnO_4 nanoparticles$_{recovered}$ (E_g: ∼3.62 eV) ≈ 0-D Zn_2SnO_4 nanoparticles$_{as\ prepared}$ (E_g: ∼3.51 eV) < 1-D Zn_2SnO_4 nanostructures$_{recovered}$ ($E_{g\ inverse\ spinel}$: ∼4.19 eV;

Table 1. Comparison of the Crystal Structures, Optical Properties, and Efficiencies of Photocatalytic Degradation of MB Dye of the Zn_2SnO_4 Nanomaterials at Ambient Pressure Conditions and Their Recovered Counterparts after the Pressure Treatments

	0-D nanoparticles		1-D nanostructures	
	ambient	recovered	ambient	recovered
phase(s)	I (inverse spinel)	I	I	I + HPOr (new high pressure orthorhombic)
absorption edge (nm); band gap/E_g (eV)	~353; 3.51	~342; 3.62	~322; 3.85	~296; 4.19 (I), ~368; 3.37 (HPOr)
main emission maxima (nm)	358	345	328	311 (I), 371 (HPOr)
photodegradation of MB (C/C_0) in the presence of the samples after 35 min	0.3	0.33	0.78	full degradation

$E_{g\ orthorombic}$: ~3.37 eV) (Figure S3). The efficiency is, thus, found to vary according to the suitable band gap energy of the samples with respect to the light source ($E_g \approx 3.39$ eV). Therefore, a minor downtrend in the degradation efficiencies is observed for the 0-D Zn_2SnO_4 nanoparticles after the pressure is released. In contrast, the degradation efficiencies are significantly enhanced for the recovered Zn_2SnO_4 nanostructures, where the heterojunction of the two phases, namely, inverse spinel (E_g: ~4.19 eV) and orthorhombic phase (E_g: ~3.37 eV), can effectively reduce the possibility of recombination of the photogenerated electrons and holes.[43] The optical properties and efficiencies of photocatalytic degradation of the MB dye of the Zn_2SnO_4 nanomaterials at ambient pressure conditions and the recovered counterparts after the pressure treatments are assembled together in Table 1 mentioning their respective crystal structure.

CONCLUSIONS

The impacts of the size and morphology of nanostructured Zn_2SnO_4 on their phase transformation behavior were investigated using 0-D Zn_2SnO_4 nanoparticles with an average particle size of ~7 nm and 1-D Zn_2SnO_4 nanostructures with a typical chain-like morphology with several uneven interparticle voids. Unlike previously established martensitic phase transition of spinel structures, the 0-D Zn_2SnO_4 nanoparticles with an inverse spinel structure showed no significant pressure-induced structural modification under high pressure up to ~40 GPa. On the other hand, an irreversible phase transformation was observed for the 1-D Zn_2SnO_4 inverse spinel Zn_2SnO_4 nanostructures to form a new quenchable high-pressure orthorhombic $CaFe_2O_4$-type structure. The inhomogeneously distributed pressure-induced strain relating to its distinct morphology is accounted for. Modifications of the optical band gaps and in emission properties can be seen after the pressure treatments. The photocatalytic degradation efficiencies of the original nanoparticles were compared to those of their respective pressure-recovered counterparts using the organic pollutant, MB. The pressure-recovered Zn_2SnO_4 nanostructures that have a heterojunction between the inverse spinel and the new orthorhombic phases appeared to be the most efficient photocatalyst.

EXPERIMENTAL SECTION

The 0-D Zn_2SnO_4 nanoparticles of ~7 nm size were prepared by the hydrothermal method, the most widely used technique for synthesizing nanomaterials.[50] In contrast, the dense and elongated 1-D Zn_2SnO_4 nanostructures were prepared by calcining a stoichiometric mixture of the two presynthesized reactive precursors, namely, ZnO rod-like microstructures and SnO_2 nanoparticles.[41] The explicit synthetic techniques for

these precursors are mentioned elsewhere.[41,50] The grain sizes and morphologies of the Zn_2SnO_4 nanostructures were examined by TEM analysis on a Tecnai G2 30ST. The HAADF-STEM images of the samples were taken using a JEOL JEM 2100F equipped with a CEOS-corrector. The specific surface areas of the samples were measured using the BET method on a Quantachrome Instrument (iQ3, USA) by nitrogen adsorption−desorption studies at 77 K, whereas the BJH method was followed for calculating the PSDs. XPS measurements were carried out in a PHI 5000 VersaProbe II scanning XPS microprobe (ULVAC-PHI, U.S.). High-pressure experiments were performed using a symmetric diamond anvil cell furnished with a pair of type-I diamonds with culet sizes of 300 μm. A preindented stainless-steel gasket drilled with a 120 μm diameter hole at the center was used as the sample chamber, whereas Si oil was used as the pressure transmitting medium. A small ruby chip was used as the pressure gauge, and the R1-line emission of the ruby chip was used for pressure calibration during the measurements. In situ high pressure XRD measurements were conducted on the 6D beamline at Pohang Accelerator Laboratory (PAL) using a monochromatic 18.785 keV X-ray beam (λ = 0.6600 Å) with a diameter of 100 μm. A charge-coupled device detector was used for recording the Debye rings, which were further integrated into 1-D profiles using the Fit2D program. In situ high-pressure Raman measurements were performed by an inVia Raman spectrometer with a 532 nm excitation laser and 2400 g/cm grating at the Center for High Pressure Science & Technology Advanced Research, Shanghai, China, keeping the sample conditions similar to those used for the XRD measurements. The same spectrometer was used to measure the emission spectra of the samples using a UV laser of wavelength 325 nm (IK3301R-G He−Cd Laser, K KIMMON) as the excitation source. DR spectra of the samples were measured on a UV−vis−NIR spectrometer (Shimadzu UV-3600). For a typical experiment, the photocatalytic activities of the ambient and released samples were evaluated by measuring the degradation rate of MB (Merck, Germany) dye solution. An 8 W UV lamp (UVLS-28 EL Series) with an average light intensity of 0.6 mW/cm^2 and an emitting wavelength of 365 nm (UVC, ~3.39 eV) was used as the irradiation source in a closed chamber. The dye degradation under UV light was periodically monitored by UV−vis spectroscopy (Shimadzu UV-3600).

ASSOCIATED CONTENT

ⓢ Supporting Information

The Supporting Information is available free of charge on the ACS Publications website at DOI: 10.1021/acsomega.9b01361.

Whole profile fitting of the XRD patterns of the 1-D Zn_2SnO_4 nanostructures at ~14, ~30, ~40 GPa, and after the pressure is released, scaled strain derived from the S−H equation based on the (111), (511), (220), and (440) diffraction planes of the 1-D Zn_2SnO_4 nanostructures, and absorption spectra of MB in the presence of the as-prepared and recovered 0-D Zn_2SnO_4 nanoparticles and 1-D Zn_2SnO_4 nanostructures under UV irradiation for different time intervals (PDF)

■ AUTHOR INFORMATION

Corresponding Author
*E-mail: yongjaelee@yonsei.ac.kr.

ORCID ◉
Partha Pratim Das: 0000-0001-6687-8324
P. Sujatha Devi: 0000-0002-6224-7821
Yongjae Lee: 0000-0002-2043-0804

Notes
The authors declare no competing financial interest.

■ ACKNOWLEDGMENTS

■ REFERENCES

(1) Hadjipanayis, G. C.; Siegel, R. W. *Nanophase Materials: Synthesis-Properties-Applications*; Kluwer Academic: Dordrecht, 1994.

(2) Fiorani, D.; Sberveglieri, G. *Fundamental Properties of Nanostructured Materials*; World Scientific: Singapore, 1994.

(3) *Springer Handbook of Nanotechnology*; Bhustan, B., Ed.; Springer: New York, 2007.

(4) *CRC Materials Science and Engineering Handbook*; Shackelford, J. F., Alexander, W., Park, J. S., Eds.; CRC Press: Boca Raton, 1994.

(5) *Nanoparticles and the Environment in Reviews in Mineralogy and Geochemistry*; Banfield, J. A., Navrotsky, A., Eds.; Mineralogical Society of America: New York, 2001; p 44.

(6) Siegel, R. W. Nanostructured materials -mind over matter-. *Nanostruct. Mater.* 1993, 3, 1−18.

(7) Gleiter, H. Nanostructured materials: basic concepts and microstructure. *Acta Mater.* 2000, 48, 1−29.

(8) Palosz, B.; Stel makh, S.; Grzanka, E.; Gierlotka, S.; Pielaszek, R.; Bismayer, U.; Werner, S.; Palosz, W. High pressure x-ray diffraction studies on nanocrystalline materials. *J. Phys.: Condens. Matter* 2004, 16, S353−S377.

(9) Zhang, H.; Cheng, B.; Li, Q.; Liu, B.; Mao, Y. Morphology-Tuned Phase Transitions of Horseshoe Shaped $BaTiO_3$ Nanomaterials under High Pressure. *J. Phys. Chem. C* 2018, 122, 5188−5194.

(10) Lü, X.; Yang, W.; Quan, Z.; Lin, T.; Bai, L.; Wang, L.; Huang, F.; Zhao, Y. Enhanced Electron Transport in Nb-Doped TiO_2 Nanoparticles via Pressure-Induced Phase Transitions. *J. Am. Chem. Soc.* 2014, 136, 419−426.

(11) Zhang, H.; Ke, F.; Li, Y.; Wang, L.; Liu, C.; Zeng, Y.; Yao, M.; Han, Y.; Ma, Y.; Gao, C. Anomalous Structural Transition and Electrical Transport Behaviors in Compressed Zn_2SnO_4: Effect of Interface. *Sci. Rep.* 2015, 5, 14417.

(12) Park, S.-w.; Jang, J.-t.; Cheon, J.; Lee, H.-H.; Lee, D. R.; Lee, Y. Shape-Dependent Compressibility of TiO_2 Anatase Nanoparticles. *J. Phys. Chem. C* 2008, 112, 9627−9631.

(13) Tang, S.; Li, Y.; Zhang, J.; Zhu, H.; Dong, Y.; Zhu, P.; Cui, Q. Effects of microstructures on the compression behavior and phase transition routine of In_2O_3 nanocubes under high pressures. *RSC Adv.* 2015, 5, 85105−85110.

(14) Li, Q.-J.; Liu, B.-B. High pressure structural phase transitions of TiO_2 nanomaterials. *Chin. Phys. B* 2016, 25, 076107.

(15) Bruchez, M., Jr.; Moronne, M.; Gin, P.; Weiss, S.; Alivisatos, A. P. Semiconductor nanocrystals as fluorescent biological labels. *Science* 1998, 281, 2013−2016.

(16) Aricò, A. S.; Bruce, P.; Scrosati, B.; Tarascon, J.-M.; van Schalkwijk, W. Nanostructured materials for advanced energy conversion and storage devices. *Nat. Mater.* 2005, 4, 366−377.

(17) Skumryev, V.; Stoyanov, S.; Zhang, Y.; Hadjipanayis, G.; Givord, D.; Nogués, J. Beating the superparamagnetic limit with exchange bias. *Nature* 2003, 423, 850−853.

(18) Fang, X.; Bando, Y.; Gautam, U. K.; Ye, C.; Golberg, D. Inorganic semiconductor nanostructures and their field-emission applications. *J. Mater. Chem.* 2008, 18, 509−522.

(19) Jie, J.; Zhang, W.; Bello, I.; Lee, C.-S.; Lee, S.-T. One-dimensional II-VI nanostructures: Synthesis, properties and optoelectronic applications. *Nano Today* 2010, 5, 313−336.

(20) Ackland, G. J. High-pressure phases of group IV and III-V semiconductors. *Rep. Prog. Phys.* 2001, 64, 483−516.

(21) Tolbert, S. H.; Alivisatos, A. P. High-Pressure Structural Transformations in Semiconductor Nanocrystals. *Annu. Rev. Phys. Chem.* 1995, 46, 595−625.

(22) Gupta, D. C.; Rana, P. Study of semiconducting nanomaterials under pressure. *J. Mol. Model.* 2012, 18, 3341−3350.

(23) Tolbert, S. H.; Alivisatos, A. P. The wurtzite to rock salt structural transformation in CdSe nanocrystals under high pressure. *J. Chem. Phys.* 1995, 102, 4642−4656.

(24) He, Y.; Liu, J. F.; Chen, W.; Wang, Y.; Wang, H.; Zeng, Y. W.; Zhang, G. Q.; Wang, L. N.; Liu, J.; Hu, T. D.; Hahn, H.; Gleiter, H.; Jiang, J. Z. High-pressure behavior of SnO_2 nanocrystals. *Phys. Rev. B: Condens. Matter Mater. Phys.* 2005, 72, 212102.

(25) Liu, J. F.; He, Y.; Chen, W.; Zhang, G. Q.; Zeng, Y. W.; Kikegawa, T.; Jiang, J. Z. Bulk Modulus and Structural Phase Transitions of Wurtzite CoO Nanocrystals. *J. Phys. Chem. C* 2007, 111, 2−5.

(26) Jiang, J. Z.; Olsen, J. S.; Gerward, L.; Mørup, S. Enhanced bulk modulus and reduced transition pressure in γ-Fe_2O_3 nanocrystals. *Europhys. Lett.* 1998, 44, 620−626.

(27) Wang, Z.; Tait, K.; Zhao, Y.; Schiferl, D.; Zha, C.; Uchida, H.; Downs, R. T. Size-Induced Reduction of Transition Pressure and Enhancement of Bulk Modulus of AlN Nanocrystals. *J. Phys. Chem. B* 2004, 108, 11506−11508.

(28) Pischedda, V.; Hearne, G. R.; Dawe, A. M.; Lowther, J. E. Ultrastability and Enhanced Stiffness of ~6 nm TiO_2 Nanoanatase and Eventual Pressure-Induced Disorder on the Nanometer Scale. *Phys. Rev. Lett.* 2006, 96, 035509.

(29) Yan, X.; Ren, X.; He, D.; Chen, B.; Yang, W. Mechanical behaviors and phase transition of Ho_2O_3 nanocrystals under high pressure. *J. Appl. Phys.* 2014, 116, 033507.

(30) Hearne, G. R.; Zhao, J.; Dawe, A. M.; Pischedda, V.; Maaza, M.; Nieuwoudt, M. K.; Kibasomba, P.; Nemraoui, O.; Comins, J. D. Effect of grain size on structural transitions in anatase TiO_2: A Raman spectroscopy study at high pressure. *Phys. Rev. B: Condens. Matter Mater. Phys.* 2004, 70, 134102.

(31) Al-Khatatbeh, Y.; Lee, K. K. M.; Kiefer, B. Compressibility of Nanocrystalline TiO_2 Anatase. *J. Phys. Chem. C* 2012, 116, 21635−21639.

(32) Chen, C.; Herhold, A. B.; Johnson, C. S.; Alivisatos, A. P. Size Dependence of Structural Metastability in Semiconductor Nanocrystals. *Science* 1997, 276, 398−401.

(33) Xiao, G.; Wang, K.; Zhu, L.; Tan, X.; Qiao, Y.; Yang, K.; Ma, Y.; Liu, B.; Zheng, W.; Zou, B. Pressure-Induced Reversible Phase Transformation in Nanostructured Bi_2Te_3 with Reduced Transition Pressure. *J. Phys. Chem. C* 2015, 119, 3843−3848.

(34) Wang, L.; Yang, W.; Ding, Y.; Ren, Y.; Xiao, S.; Liu, B.; Sinogeikin, S. V.; Meng, Y.; Gosztola, D. J.; Shen, G.; Hemley, R. J.; Mao, W. L.; Mao, H. K. Size-Dependent Amorphization of Nanoscale Y_2O_3 at High Pressure. *Phys. Rev. Lett.* 2010, 105, 095701.

(35) Wang, Q.; He, D.; Peng, F.; Lei, L.; Liu, P.; Yin, S.; Wang, P.; Xu, C.; Liu, J. Unusual Compression Behavior of Nanocrystalline CeO_2. *Sci. Rep.* **2015**, *4*, 4441.

(36) Das, P. P.; Samanta, S.; Wang, L.; Kim, J.; Vogt, T.; Devi, P. S.; Lee, Y. Redistribution of native defects and photoconductivity in ZnO under pressure. *RSC Adv.* **2019**, *9*, 4303−4313.

(37) Liu, B.; Yao, M.; Liu, B.; Li, Z.; Liu, R.; Li, Q.; Li, D.; Zou, B.; Cui, T.; Zou, G.; Liu, J.; Chen, Z. High-Pressure Studies on CeO_2 Nano-Octahedrons with a (111)-Terminated Surface. *J. Phys. Chem. C* **2011**, *115*, 4546−4551.

(38) Li, Q.; Cheng, B.; Tian, B.; Liu, R.; Liu, B.; Wang, F.; Chen, Z.; Zou, B.; Cui, T.; Liu, B. Pressure-induced phase transitions of TiO_2 nanosheets with high reactive {001} facets. *RSC Adv.* **2014**, *4*, 12873−12877.

(39) Wang, Z.; Daemen, L. L.; Zhao, Y.; Zha, C. S.; Downs, R. T.; Wang, X.; Wang, Z. L.; Hemley, R. J. Morphology-tuned wurtzite-type ZnS nanobelts. *Nat. Mater.* **2005**, *4*, 922−927.

(40) Baruah, S.; Dutta, J. Zinc stannate nanostructures: hydrothermal synthesis. *Sci. Technol. Adv. Mater.* **2011**, *12*, 013004.

(41) Das, P. P.; Devi, P. S. Formation of Self-Assembled Defect-Free Zn_2SnO_4 Nanostructures from Binary Oxides without the Kirkendall Effect. *Inorg. Chem.* **2014**, *53*, 10797−10799.

(42) Das, P. P.; Roy, A.; Sujatha Devi, P. Zn_2SnO_4 as an Alternative Photoanode for Dye Sensitized Solar Cells: Current Status and Future Scope. *Trans. Indian Ceram. Soc.* **2016**, *75*, 147−154.

(43) Das, P. P.; Roy, A.; Tathavadekar, M.; Devi, P. S. Photovoltaic and photocatalytic performance of electrospun Zn_2SnO_4 hollow fibers. *Appl. Catal., B* **2017**, *203*, 692−703.

(44) Gracia, L.; Beltrán, A.; Andrés, J. A Theoretical Study on the Pressure-Induced Phase Transitions in the Inverse Spinel Structure Zn_2SnO_4. *J. Phys. Chem. C* **2011**, *115*, 7740−7746.

(45) Shen, X.; Shen, J.; You, S. J.; Yang, L. X.; Tang, L. Y.; Li, Y. C.; Liu, J.; Yang, H.; Zhu, K.; Liu, Y. L.; Zhou, W. Y.; Jin, C. Q.; Yu, R. C.; Xie, S. Phase transition of nanowires under high pressure. *J. Appl. Phys.* **2009**, *106*, 113523.

(46) Šepelák, V.; Becker, S. M.; Bergmann, I.; Indris, S.; Scheuermann, M.; Feldhoff, A.; Kubel, C.; Bruns, M.; Sturzl, N.; Ulrich, A. S.; Ghafari, M.; Hahn, H.; Grey, C. P.; Beckerbk, K. D.; Heitjans, P. Nonequilibrium structure of Zn_2SnO_4 spinel. *J. Mater. Chem.* **2012**, *22*, 3117−3126.

(47) Chen, J.; Weidner, D. J.; Parise, J. B.; Vaughan, M. T.; Raterron, P. Observation of Cation Reordering during the Olivine-Spinel Transition in Fayalite by In Situ Synchrotron X-Ray Diffraction at High Pressure and Temperature. *Phys. Rev. Lett.* **2001**, *86*, 4072−4075.

(48) Wang, Z.; Lazor, P.; Saxena, S. K.; Artioli, G. High-Pressure Raman Spectroscopic Study of Spinel ($ZnCr_2O_4$). *J. Solid State Chem.* **2002**, *165*, 165−170.

(49) Wang, Z.; Lazor, P.; Saxena, S. K.; O'Neill, H. S. C. High pressure Raman spectroscopy of ferrite $MgFe_2O_4$. *Mater. Res. Bull.* **2002**, *37*, 1589−1602.

(50) Das, P. P.; Roy, A.; Agarkar, S.; Devi, P. S. Hydrothermally synthesized fluorescent Zn_2SnO_4 nanoparticles for dye sensitized solar cells. *Dyes Pigm.* **2018**, *154*, 303−313.

(51) Sohlberg, K.; Pennycook, T. J.; Zhou, W.; Pennycook, S. J. Insights into the physical chemistry of materials from advances in HAADF-STEM. *Phys. Chem. Chem. Phys.* **2015**, *17*, 3982−4006.

(52) Esser, B. D.; Hauser, A. J.; Williams, R. E. A.; Allen, L. J.; Woodward, P. M.; Yang, F. Y.; McComb, D. W. Quantitative STEM Imaging of Order-Disorder Phenomena in Double Perovskite Thin Films. *Phys. Rev. Lett.* **2016**, *117*, 1761019.

(53) Wei, S.-H.; Zhang, S. First-principles study of cation distribution in eighteen closed-shell $A^{II}B_2^{III}O_4$ and $A^{IV}B_2^{II}O_4$ spinel oxides. *Phys. Rev. B: Condens. Matter Mater. Phys.* **2001**, *63*, 045112.

(54) Yamanaka, T.; Uchida, A.; Nakamoto, Y. Structural transition of post-spinel phases $CaMn_2O_4$, $CaFe_2O_4$, and $CaTi_2O_4$ under high pressures up to 80 GPa. *Am. Mineral.* **2008**, *93*, 1874−1881.

(55) Kyono, A.; Ahart, M.; Yamanaka, T.; Gramsch, S.; Mao, H.-k.; Hemley, R. J. High-pressure Raman spectroscopic studies of ulvöspinel Fe_2TiO_4. *Am. Mineral.* **2011**, *96*, 1193−1198.